Computers and Fluids 126 (2016) 91–101

Contents lists available at ScienceDirect

Computers and Fluids

journal homepage: www.elsevier.com/locate/compfluid

Assessment of turbulence model performance: Large streamline curvature and integral length scales

Xiaoyu Yang*, Paul G. Tucker

Department of Engineering, University of Cambridge, Trumpington Street, Cambridge CB2 1PZ, United Kingdom

ARTICLE INFO

Article history:
Received 15 December 2014
Revised 8 September 2015
Accepted 24 November 2015
Available online 10 December 2015

Keywords:
Turbulence
Turbulence modelling
Streamline curvature
Reynolds-stress models
Eddy-viscosity models
Reynolds-averaged Navier–Stokes simulation
Computational fluid dynamics

ABSTRACT

For the flow over curved surfaces, an extra wall-normal pressure gradient is imposed to the flow through excessive surface pressure, such that the flow turns in alignment with the surface. In turn, turbulent fluctuations are suppressed over the convex surface; whereas, they are enhanced over the concave. Recently, the direct numerical simulation (DNS) of turbulent channel flow experiencing a 60 degree circular bend shows highly complex flow phenomena. Particularly, the mean flow properties are directly related to the channel geometry; in the impulse response of the mean flow to the step change of streamline curvature, sudden changes in mean strain rate and extra rates of strain emerge. This mean flow process is prior to the response of the turbulence structures. Due to the large streamline curvature, the underlying turbulence lagging mechanism and the stress strain misalignment are difficult to model. For this, the new DNS data for the wall bounded flow with high streamline curvature and large integral length scales is used to explore RANS performance. For eddy-viscosity models, this leads to the Boussinesq approximation being questionable. Also, for a Reynolds-stress model (RSM) with closure approximations applicable to homogeneous turbulent flows that are nearly in equilibrium, the current case can result in substantial predictive error. This is because of, for example, the linear approximation for the rapid pressure–strain correlation. To help move towards better turbulence modelling, Reynolds-averaged Navier–Stokes (RANS) predictions are compared for the same flow configuration as the DNS, using some popular turbulent models. These models include the second-order closure with the stress-ω formulation, the standard $k-\omega$ and the Menter's shear-stress transport (SST) models, the standard Spalart–Allmaras (S-A) model with and without the corresponding strain–vorticity correction. As expected, overall, the RSM provides closer predictions to the DNS data than the selected eddy-viscosity models, even though the predictive accuracy needs to be further improved. Potentially, a non-linear constitutive relation or second-order closure, incorporating a relaxation approximation for the lagging mechanism, may lead to a remedy for the current non-equilibrium flow. Moreover, all models would also benefit from sensitisation to the impact of the large integral length scales.

1. Introduction

Relative to flow over a flat surface, when experiencing curved boundaries, more complexity emerges from the turbulence structures. Depending on the shape of such a viscous surface, extra momentum is imposed to the flow through an excessive wall pressure distribution. In such a way, the flow is forced to turn in alignment with the solid boundary. This usually results in static pressure gradient and dynamic head variation. Naturally, the shear layer structures are distorted due to extra strain rates. Early efforts on this subject are reviewed by Bradshaw [1–3].

In addition to the usual productive shear $\partial U/\partial y$ driving the wall turbulence, to gain some insight about modelling extra strain rates, the impulsive response of the boundary layer to high surface curvature was tested by Smits et al. [4] in their boundary layer experiment of 20 and 30 degree bends. Characteristic structural changes were investigated based on analysis of single-point double and triple velocity products. The various forms of the shear-stress parameters were increased over the concave side, and thereafter decayed further downstream. On the convex side, large reductions were found, before downstream recovery. Notably, in these experiments, separation is avoided. In the companion, after transition, the alteration due to the lateral divergence $\partial W/\partial z$ was confirmed in almost the same way

* Corresponding author. Tel.: +44 1223 337 582; fax: +44 1223 332 662.
E-mail address: xiaoyu.yang@alumni.stanford.edu, xiaoyu.yang.alumni.cambridge@outlook.com (X. Yang).

http://dx.doi.org/10.1016/j.compfluid.2015.11.010

as the longitudinal curvature above. Where, W is the mean velocity in the spanwise direction z. This is given by Smits et al. [5].

The corresponding asymptotic response to the streamline curvature was investigated in the pioneering experiments by So and Mellor [6–8]. Strikingly, in this experiment [6,9], substantial laminarisation was observed over a convex surface under laboratory condition. Such a phenomenon is also common in meteorology. As originally determined by Richardson [10] based on atmospheric data, for this phenomenon, above a critical Richardson number Ri_{cr} turbulence collapses.

Usually, the gradient Richardson number provides a measure of the ratio between typical body (centrifugal or buoyant) force and typical inertia force, i.e. Ri = typical body force/typical inertia force. It also reflects the dimensionless rotational/angular frequency, i.e. the square of the ratio of the mean rotational frequency U/R to the mean vorticity $\partial U/\partial r$. For curved shear flow, this may be defined as [7,11]

$$Ri = S_C \cdot (1 + S_C) \tag{1}$$

where,

$$S_C = \frac{\dfrac{2k_cU}{1+k_cy} - 2\Omega}{\dfrac{\partial U}{\partial y} - \dfrac{k_cU}{1+k_cy}} \tag{2}$$

and $k_c = 1/R$ is the surface curvature, y is the wall-normal distance, and Ω is the magnitude of the rotational tensor. Alternatively, the flux Richardson number measures the ratio of the turbulence kinetic energy (TKE) production magnitude due to body force and mean shear. This may be written as the equation below.

$$Ri_f = S_C/(1 + S_C) \tag{3}$$

Also, in addition to the usual production term for the Reynolds shear stress, for curved shear flow, another term is active. The corresponding production ratio, i.e. the stress Richardson number, may be written as $Ri_s = (\overline{v'_s v'_s}/\overline{v'_n v'_n}) \cdot Ri_f$, where v'_s and v'_n are the streamwise and the wall-normal velocity fluctuations. Mostly, the gradient and/or flux Richardson number is used as a measure for the significance of the streamline curvature effect.

On the other hand, for the early effort to model the turbulence reduction mechanism, Prandtl [12] reduced the eddy-viscosity/mixing-length when the global rotational rate is comparable to the local mean shear. Based on the Richardson number

$$Ri = (U/R)/(\partial U/\partial r), \tag{4}$$

multiplying the mixing length by a factor $F = 1 - \beta \cdot Ri$ was proposed for curved flow, where $\beta = 1/4$. This is analogous to buoyancy effect. However, this model under-predicts the observations, for example those given by Wilcken [13] and Wattendorf [14]. For mild/small streamline curvature $\delta/R \sim 0.01$, substantial improvement was made by Bradshaw [11] based on an approximate gradient Richardson number, i.e. $F = 1 - \beta \cdot Ri_A$, where

$$Ri_A = 2S_A \cdot (1 + S_A) \tag{5}$$

and

$$S_A = \left(\frac{k_cU}{1+k_cy}\right) \Big/ \left(\frac{\partial U}{\partial y}\right). \tag{6}$$

This is in analogy to the Monin–Oboukhov [15] formula for buoyant flows. For such early models, inadequacy arises, for example, when pressure gradient effects cannot be neglected. For moderate streamline curvature $\delta/R \sim 0.1$, So and Mellor [6,7,9] derived an eddy-viscosity function from the Reynolds-stress equations, including the pressure-velocity correlation terms, etc.. This gives a turbulence velocity scale. Accordingly, the calculated boundary layer development was found in good agreement with their measurements. Meanwhile, the occurrence of laminarisation was also accurately predicted. The model was shown to be valid for $-0.21 \le Ri_f \le 0.21$, where, Ri_f is defined to be a flux Richardson number. Also, the critical value was found to be $Ri_{f,cr} = 0.215$.

In the succeeding efforts to predict large curvature effects, the focus was on the two-dimensional curved boundary layer equations, instead of the thin shear layer approximation neglecting static pressure variation. For example, this is shown by So and Mellor [16,17] using an ASM with $k - \epsilon$ model. Additionally, using the universal log-linear law for the near wall region, So [18] further illustrated the close analogy between buoyancy and streamline curvature. Meanwhile, for the standard $k - \omega$ model, Wilcox and Chambers [19] proposed a centrifugal acceleration term to account for surface curvature effect. This originated from the exact $\overline{v'v'}$ equation, based on the classical stability arguments advanced by von Karman [20]. The corresponding model predictions are much closer to So and Mellor's measurements [6] than the standard model [21]. Similarly, Launder, Priddin and Sharma [22] proposed a correction term for the $k - \epsilon$ model based on a turbulence Richardson number similar to the Prandtl's formulation above. Such curvature corrections usually result from the analysis of the full Reynolds-stress equations. The suitability of second-moment closure is investigated, for example, by Gibson et al. [23]. A comprehensive overview on modelling curvature effects has been given by Lakshminarayana [24]. These early modelling efforts, as well as the characteristic alterations in the mean and turbulent properties, are well introduced by Moser and Moin [25,26] where Direct Numerical Simulation (DNS) is undertaken for mild curvature. Also, scenarios related to non-linear constitutive relations and second-order closures are discussed by Wilcox [21,27,28]. Later development on analysis and modelling for the longitudinal curvature effects are comprehensively reviewed by Patel and Sotiropoulos [29], and the corresponding transverse curvature effects are reviewed by Piquet and Patel [30]. Recent advances and applications with non-linear eddy-viscosity models and second-moment closure are outlined by Leschziner [31].

Lately, while studying aero engine intake flow physics, the Richardson number above, i.e. Eq. (4), is used by Oriji and Tucker [32] as an indication of the corresponding centrifugal effects for turbulence modelling. For this Richardson number, U is the mean tangential velocity aligned with a flow streamline, and R is the corresponding radius of the streamline curvature. Then, the number is scaled by the freestream velocity and the boundary layer thickness. Notably, the streamline curvature effects are of fundamental importance for such flow physics. This is equally evident for aerodynamic design of compressor and turbine blades, as well as aerofoils. However, the efforts to understand and predict such flow physics are far from complete.

For this, recently, DNS is undertaken for fully developed channel flow experiencing a 60 degree circular bend [33]. Notably, for this large streamline curvature case, over the convex surface ($\delta/R = 1/6$), laminarisation, the succeeding laminar separation and induced transition, and then turbulence recovery, are directly observed; turbulence enhancement over the concave surface is also evident. These sequential flow behaviours are essentially altered by the production rate P_{12} of the Reynolds shear stress. These observations are qualitatively similar to the early experimental observations. In the following, to explore the performance of turbulence models, some popular Reynolds-stress (RSM) and eddy-viscosity models are benchmarked, and possible improvements are suggested.

Notably the data in [33] is for flow over a curved surface exposed to large upstream integral length scales. This is an important aspect of the current contribution aimed at understanding the performance of RANS models. Flows over curved surfaces subjected to large external integral length scales occur in many areas of industrial application - see for example [34]. Full details of the 6th-order finite difference

incompressible DNS involving 8 million cell grids are given in [33]. Notably, this paper connects with the companion paper [35] where large integral length scales exposed to acceleration are explored.

2. Turbulence models

For flow over a curved surface, to certain degree, the pressure gradient alters the turbulence behaviour. This usually results in laminarisation, turbulence enhancement, and even turbulence recovery through separation induced transition. Without proper correction/treatment, linear eddy-viscosity models are generally inadequate to predict such streamline curvature effects. On the contrary, the second-order closures, solving extra partial differential equations for the Reynolds stresses, are considered to be more reliable to delineate such flow physics [36,37]. In the modelled Reynolds-stress transport equations, the effects of the system rotation and/or streamline curvature are imitated by the corresponding explicit terms [26]. Whereas, eddy-viscosity models in the baseline form are primarily constructed based on the flat wall production mechanism provoked by the usual mean shear $\partial U/\partial n$ in the wall-normal direction n. As has been shown by the DNS [33], the impact of streamline curvature can be more significant, with respect to the expectation based on early numerical and experimental data. For better turbulence modelling, Reynolds-averaged Navier–Stokes (RANS) simulations are performed, for the same curved channel geometry, at a low Reynolds number the same as this DNS. Through these simulations, some of the available models, as well as the corresponding streamline curvature corrections, are benchmarked regarding to the DNS data.

These selected widely-used RANS models are as follows: the second-order closure/RSM with the stress-ω formulation [28,38–41], the standard $k-\omega$ model [28] and the Menter's SST model [42–45], the standard Spalart–Allmaras (S-A) model [46] and the corresponding strain–vorticity correction [47]. This latter correction is generally referred to as the approximate Spalart–Allmaras rotational correction (ASARC). This reduces the eddy-viscosity/turbulence when the mean rate of rotation exceeds that of the strain; the standard formulation for the production of the modified turbulent viscosity $\tilde{\nu}$ is altered as the following Eq. (7). This results in more accurate predictions on the effects of rotation and streamline curvature. The production term for ASARC takes the form below

$$S_{S-A} = \mid \Omega_{ij} \mid + C_{prod} \cdot min(0, \mid S_{ij} \mid - \mid \Omega_{ij} \mid), \tag{7}$$

where $C_{prod} = 2.0$, $\mid \Omega_{ij} \mid = \sqrt{2\Omega_{ij}\Omega_{ij}}$, and $\mid S_{ij} \mid = \sqrt{2S_{ij}S_{ij}}$. Ω_{ij} and S_{ij} are the mean rotation and strain tensor, respectively. Notably, when C_{prod} is set to be 0, the standard form is recovered.

The detailed description on these selected models have been given, for example, by Wilcox [28] or the ANSYS-FLUENT theory guide [48]. Also, a recent assessment on such models has been summarised by Nichols [49]. Particularly, it has been shown that this ASARC modification gives RANS results similar to that of the Spalart–Shur's correction [36,37] for rotation and curvature (SARC) [49]. This latter case is not studied here, due to the expensive evaluation of a Lagrangian derivative of the strain tensor.

For the RSM with the stress-ω formulation [28], the ω equation of specific dissipation rate, identical to the Wilcox (2006) $k-\omega$ model, is used as the scale-determining equation. For the corresponding modelled Reynolds-stress transport equations, the underlying k equation is also identical to the above $k-\omega$ model. As employed in this second-moment closure, for the exact incompressible transport equations for the (specific) Reynolds stresses $\tau_{ij} = \overline{u_i'u_j'}$, i.e. Eq. (8), the approximations are as follows: the dissipation tensor ϵ_{ij} is approximated based on the Kolmogorov [50] hypothesis of local isotropy; the Daly and Harlow [51] simple approximation is employed for turbulent transport terms C_{ijk}. Meanwhile, for the pressure–strain correlation $\Pi_{ij} = A_{ij} + M_{ijkl} \cdot \partial U_k/\partial x_l$, the slow pressure strain A_{ij} is modelled using Rotta's postulation [52,53], and the Launder, Reece and Rodi [39] linear approximation is used for the rapid pressure strain $M_{ijkl} \cdot \partial U_k/\partial x_l$. Notably, with the scale-determining ω equation, the stress-ω formulation does not require a wall-reflection/pressure-echo term such as that used for the RSM model based on the ϵ equation. Also, similar to the $k-\omega$ model, this second-moment closure has the potential for excellent predictions over a wide range of turbulent flows, particularly, for flows over curved surfaces [48]. The Reynolds stress transport equations take the form below

$$\frac{\partial \tau_{ij}}{\partial t} + U_k \frac{\partial \tau_{ij}}{\partial x_k} = P_{ij} - \epsilon_{ij} + \Pi_{ij} + \frac{\partial}{\partial x_k}\left[\nu_0 \frac{\partial \tau_{ij}}{\partial x_k} - C_{ijk}\right] \tag{8}$$

where,

$$P_{ij} = -\tau_{ik}\frac{\partial U_j}{\partial x_k} - \tau_{jk}\frac{\partial U_i}{\partial x_k} \tag{9}$$

$$\epsilon_{ij} = 2\nu_0 \overline{\frac{\partial u_i'}{\partial x_k}\frac{\partial u_j'}{\partial x_k}} \tag{10}$$

$$\Pi_{ij} = \overline{\frac{p'}{\rho_0}\left(\frac{\partial u_i'}{\partial x_j} + \frac{\partial u_j'}{\partial x_i}\right)} \tag{11}$$

$$\rho_0 C_{ijk} = \rho_0 \overline{u_i'u_j'u_k'} + \overline{p'u_i'}\delta_{jk} + \overline{p'u_j'}\delta_{ik} \tag{12}$$

3. Numerical methods

The RANS simulations are performed using the Rolls Royce HYDRA [54,55] compressible Navier–Stokes solver and the ANSYS-FLUENT (Version 13) [48] pressure based incompressible solver. For the former, under the compressible solver framework, the four-stage Runge–Kutta time integration and the second order Roe's scheme are used for temporal and spatial discretisation, together with a low Mach number pre-conditioning and a four-level multi-grid cycle. For the latter, the pressure terms are chosen to be coupled with velocity field through the pseudo-transient time integration. For better numerical accuracy, the combination of the spatial discretisation schemes are the least-square cell based gradient term, the second-order pressure term, and the third-order MUSCL scheme for the momentum and other turbulence-model terms. The low-Re correction/viscous damping is employed for all the benchmarked models. Also, the viscous sublayer is directly resolved using the standard no-slip wall boundary condition; for the upstream fully developed section, the first grid spacing immediately adjacent to the wall is below the wall unit, i.e. $\Delta d_{1st}^{+} \simeq 0.36$. Also, to ensure all the essential mean characteristic changes are captured, the wall-normal grid uses 51 nodes. This is about half of the number used for the DNS. These are considered to be sufficient to provide grid independent solutions. To ensure this, a grid independence study has been performed. For the RSM which is expected to have the greatest sensitivity to grid, the average profile change for the mean velocities is around 0.1% and the change in turbulence quantities around 2% for a grid doubled in all directions. For the models involving less equations and hence gradients, smaller changes are expected.

Also, for the upstream incoming flow, the stagnation and static pressure difference, through the standard pressure inlet boundary condition, is used to develop the desired flow properties. The standard outflow boundary condition is applied to the channel exit. These boundary conditions are shown in the following Fig. 1. Besides, for assessment, the ASARC result is also compared using the Rolls Royce

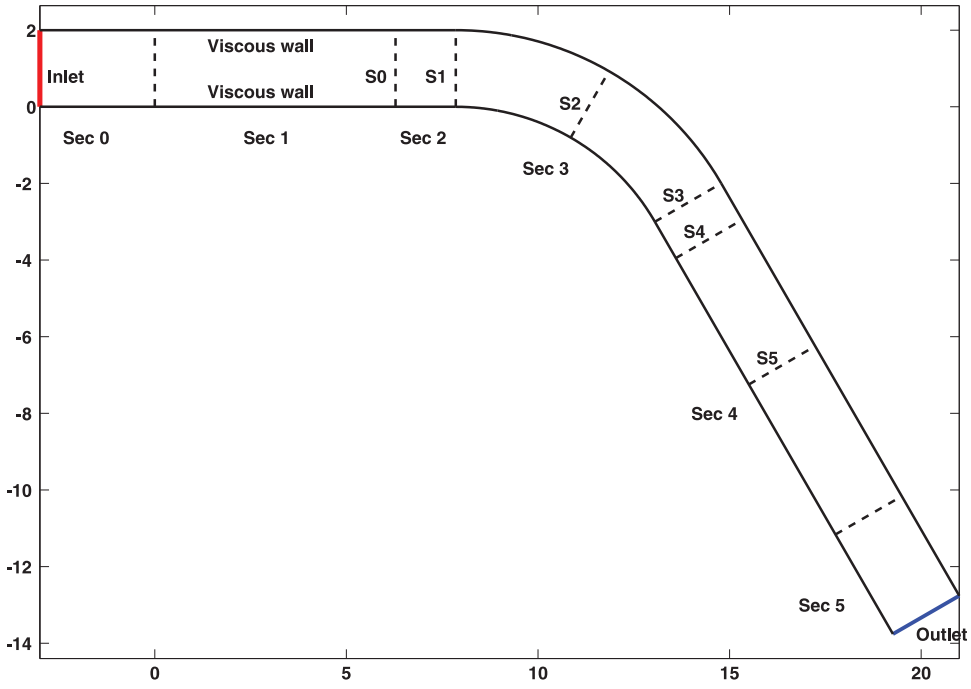

Fig. 1. Schematic of the actual simulated 60 degree circularly bent channel. (Note: the streamwise lengths for the upstream inlet section (Sec 0) and the downstream outlet section (Sec 5) are 120δ and 30δ, respectively. These are not shown in the figure. Also, the half channel height δ is scaled to be unity, and the axes are equal.).

HYDRA. For all the following results, the iterative convergence criteria is taken to be 1×10^{-6} for all the scaled residuals.

4. Flow configuration

As shown in Fig. 1, for the current RANS study, the actual simulated two-dimensional curved channel geometry is exactly the same as the cross-section of the DNS case [33]. It contains the upstream fully developed region (Sec 1), the immediate upstream guide section (Sec 2), the 60 degree circularly bent test section (Sec 3), and the downstream guide section (Sec 4). Along the lower channel surface, the streamwise lengths for these sections are $L_1 = 2\pi\,\delta$, $L_2 = 0.5\pi\,\delta$, $L_3 = 2\pi\,\delta$, and $L_4 = 3\pi\,\delta$, respectively. Where, δ is the geometrical half channel height. For the test section, in the streamwise direction, with the circumferential length of the lower convex wall $L_3 = 2\pi\,\delta$, it can be seen that the curvature is $\delta/R = 1/6$. This expands a perfect triangle. In addition, the most upstream inlet section (Sec 0 with $L_0 = 120\delta$) is used here to develop the flow, and the most downstream outlet section (Sec 5 with $L_5 = 30\delta$) for outflow. The axis origin is on the lower channel surface at the end of the upstream inlet section, and it is $2.5\pi\,\delta$ to the leading edge of the curvature. In-between, the flow is considered to be fully developed. In this way, the coordinate system is exactly the same as the DNS case. In the following, only the results close to the curvature will be examined. Besides, s, n, and z will be used as the streamwise, wall-normal, and spanwise directions, respectively, for the local curvilinear orthogonal coordinates.

To compare with the DNS data [33], for the current RANS configuration, the flow is simulated nominally at $Re_\delta = 3300$ or equivalently $Re_\tau \simeq 180$ for the upstream fully developed section. The total grid points used are 88×51. The first grid spacing above the wall is $\Delta d/h = 0.002$. For the upstream fully developed region, it is below the wall unit, i.e. $\Delta d^+_{1st} \sim 0.36$; equivalently, the viscous sublayer is resolved. The half channel height h or δ is fixed as 1 mm; under sea-level atmospheric condition, this requires the upstream centreline velocity U_{max} around 48.262 m/s, i.e. $Ma \simeq 0.142$. In the following, the corresponding RANS solutions are compared with the DNS data for the mean streamwise velocity and TKE profiles, as well as the streamwise distributions of C_f and C_p on the concave and convex surfaces. Also, the streamwise acceleration parameter and the Richardson number will be examined to gain insight about the discrepancy between the DNS and RANS results.

5. Results

Figs. 2–4 compare the mean streamwise velocity profiles at six streamwise stations. These are given in the frame (a) of Fig. 2 to the frame (b) of Fig. 4. The locations of these stations are shown in the previous Fig. 1. The first four locations are at the upstream fully developed region, the leading edge, the mid-plane, and the trailing edge of the curved section, and the other two located downstream to the curvature within and after the mean separation. The corresponding streamwise distances, along the lower channel wall, to the axes origin are given in Table 1. In these figures, the wall-normal distance, represented by y, is scaled by the half channel height/the boundary layer thickness for the upstream fully developed turbulence, and the mean velocity is scaled by the corresponding mean centreline value. Also, in this figure and the following, the full-line represents the DNS data, the dash-dot line is for the laminar profile that gives the same wall shear for the upstream fully developed region, and the RANS results are given by symbols ($\circ$ the RSM, $\square$ the $k-\omega$ SST, $\triangle$ the $k-\omega$ standard, $\triangleright$ the S-A with the strain–vorticity correction, $\triangleleft$ the S-A standard, and $+$ the HYDRA S-A with the strain–vorticity correction). As can be seen from the frame (a) of Fig. 2, for the upstream fully developed turbulence, the RANS results conform well with the DNS. Here, the standard $k-\omega$ model results in the largest deviation. It is around 5%. Also, for the lower half channel, they are able to capture the general trend superior to the end of the curvature. These are given in the frame (b) of Fig. 2 and the frame (a) of Fig. 3. Whereas, further downstream, there are relatively large discrepancies ($>$ 10%) within the mean separation and the induced transition thereafter. These are given in the frame (b) of Fig. 3, and

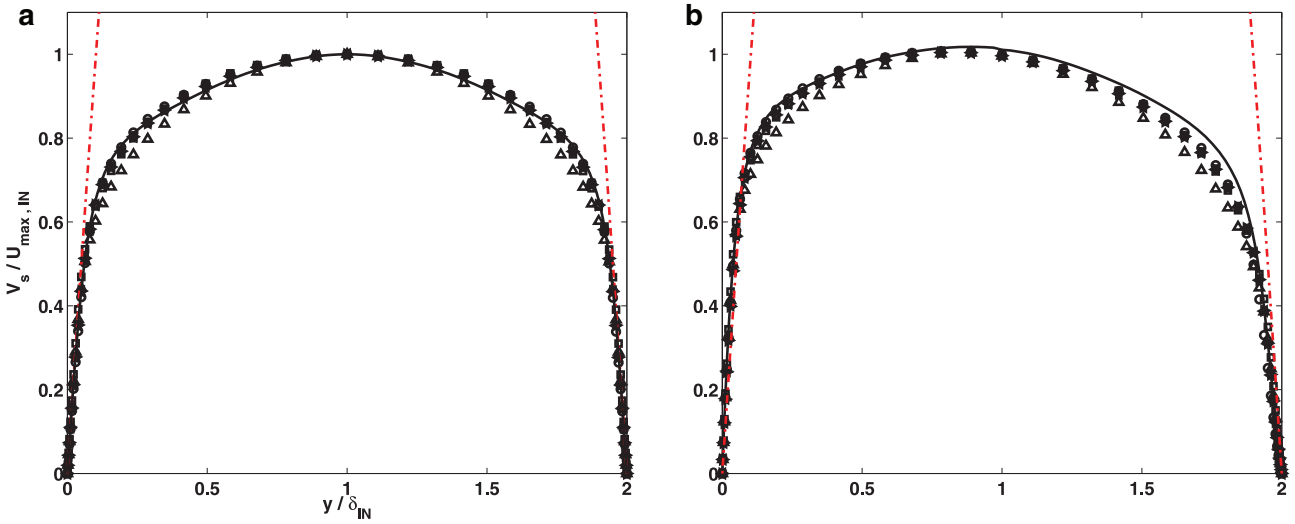

Fig. 2. Mean streamwise velocity profiles at the streamwise locations, S0 (a) and S1 (b). (− the DNS, −. the laminar, ∘ the RSM, □ the $k-\omega$ SST, △ the $k-\omega$ standard, ▷ the S-A with the strain–vorticity correction, ◁ the S-A standard, and + the HYDRA S-A with the strain–vorticity correction.).

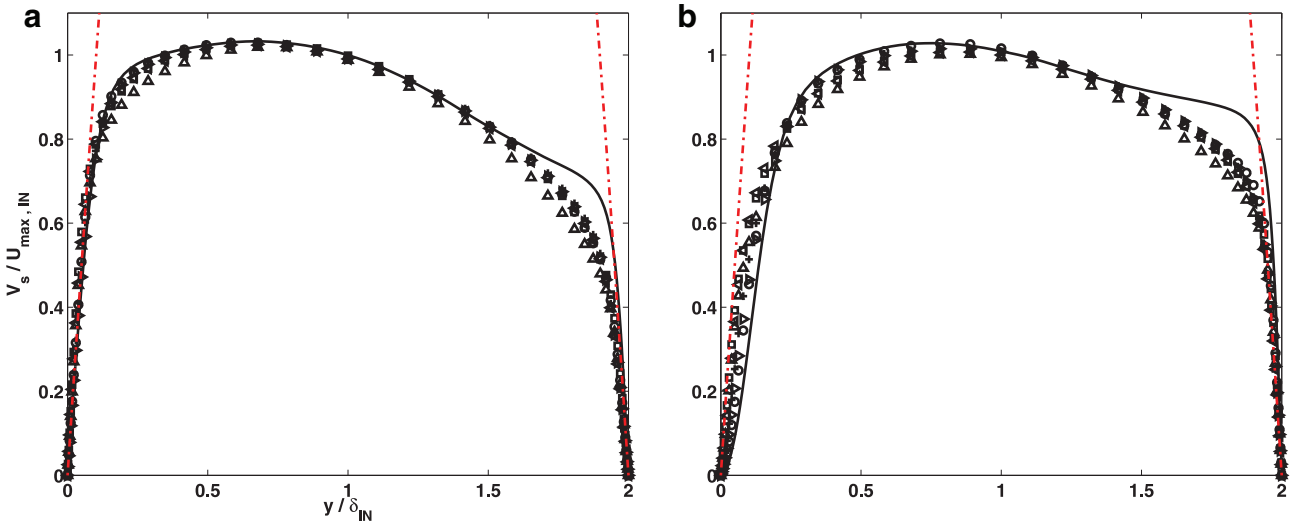

Fig. 3. Mean streamwise velocity profiles at the streamwise locations, S2 (a) and S3 (b). (− the DNS, −. the laminar, ∘ the RSM, □ the $k-\omega$ SST, △ the $k-\omega$ standard, ▷ the S-A with the strain–vorticity correction, ◁ the S-A standard, and + the HYDRA S-A with the strain–vorticity correction).

the frame (a) and (b) of Fig. 4. For the upper half channel, the deviation is even more substantial. For example, in the frame (a) of Fig. 4, all the RANS models result in more than 20% error with respect to the DNS.

More importantly, understanding the extent of the validity of the logarithmic law of the wall is essential for turbulence modelling over a curved surface [29]. Hence, for the lower half channel, the above mean streamwise velocity profiles are recast on the logarithmic abscissa. This is given in Figs. 5–7. In these figures, the wall-normal distance and the mean velocity are scaled by the corresponding local inner values. As can be seen, overall, the RSM model provides the closest approximation to the DNS. Also, the S-A model with the strain–vorticity correction (both FLUENT and HYDRA solutions) results in predictions similar to that of the RSM model. Whereas, the other eddy-viscosity models, without proper streamline curvature corrections, lead to large solution errors. Particularly, when the mean flow separates, no models are able to capture the mean velocity profile. This is shown in Figs. 6 and 7.

Correspondingly, the surface distributions of the local u_τ, C_f, and C_p are compared in Fig. 8. Five of the aforementioned streamwise stations (S1—S5) are indicated as the vertical dash-dot lines in each of these frames, as well as the following Fig. 10. As can be seen, overall, the RANS models predict the general trends for these coefficients, even though the quantitative difference can be substantial. The largest error can be more than 50%. Notably, over the bottom convex and the top concave surfaces, the wall shear stress distributions predicted by the DNS are qualitatively similar to the general trend observed in the early experiments as summarised by Moser and Moin [26]. Due to turbulence enhancement, the wall shear over the concave surface is higher than the upstream fully developed case; whereas, it is lower for the convex side. The latter is due to a reduction in turbulence. However, for this curved section, all the tested RANS models predict a relatively opposite trend. Additionally, upstream to the mean separation, the C_p distributions predicted by the RANS models match the DNS data. But, thereafter, they do not accurately reflect the turbulence recovery process through the separation

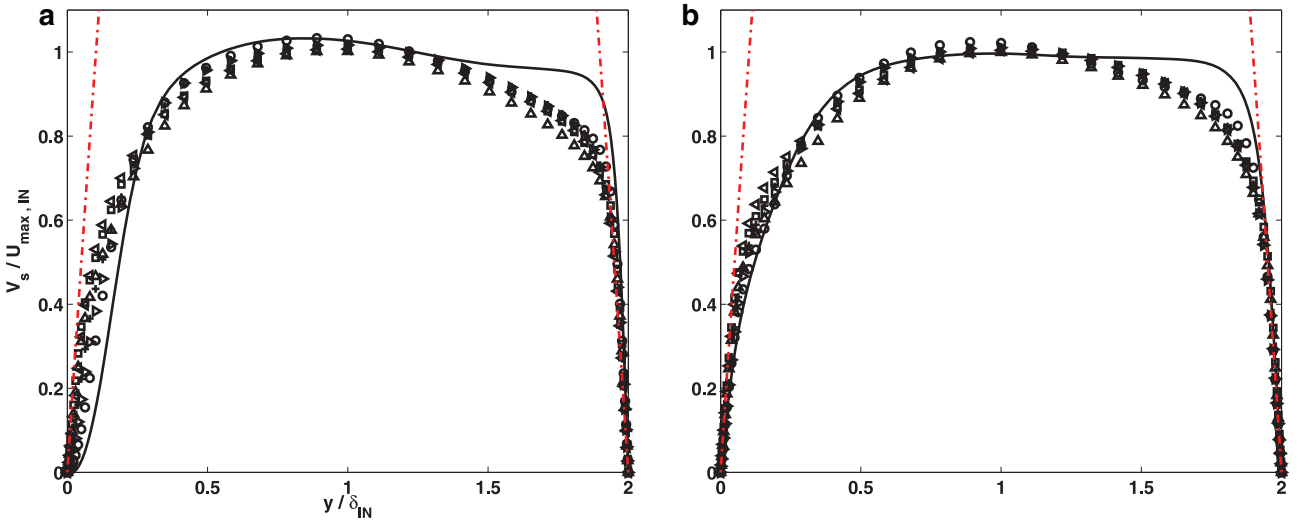

Fig. 4. Mean streamwise velocity profiles at the streamwise locations, S4 (a) and S5 (b). (– the DNS, –. the laminar, ◦ the RSM, □ the $k-\omega$ SST, △ the $k-\omega$ standard, ▷ the S-A with the strain–vorticity correction, ◁ the S-A standard, and + the HYDRA S-A with the strain–vorticity correction).

Table 1
Streamwise distance (s/δ_{IN}) to the axes origin.

Stations	s/δ_{IN}[a]
S0	Upstream
S1	2.5π
S2	3.5π
S3	4.5π
S4	15.232
S5	19.040

[a] This is measured along the lower convex channel surface.

and the succeeding induced transition. This is also the case for the C_f predictions.

In addition, Fig. 9 compares TKE profiles for the RSM and the two $k-\omega$ models at the aforementioned six streamwise locations. In this figure, the TKE is scaled using u_τ from the upstream fully developed region. As can be seen, for the incoming turbulence (the frame (a)), the predicted TKE distributions agree well with the DNS data; here, the relative error is less than 2%. Whereas, the discrepancy arises progressively, when the curvature effects accumulate. Notably, without proper correction, both the standard $k-\omega$ and the SST models have inadequate sensitivity to the streamline curvature. On the contrary, to certain degree, the RSM model reflects such effects, even though the quantitative accuracy is inadequate. For example, as shown in the frame (f), through the separation induced transition, TKE gradually recovers. Whereas, over the lower convex surface, the RSM results in around 50% error with respect to the DNS.

To see the turbulence reduction and enhancement processes, the streamwise distributions of the peak TKE for the lower and upper half channel are compared in the frame (a) of Fig. 10. The corresponding distributions of the streamwise acceleration parameter $K_s^E = (\nu_0/U_{max,IN}^2) \cdot (\partial V_s/\partial s)$ and the Richardson number $Ri = (V_s/R) \cdot (\partial V_s/\partial r)/(U_{max,IN}/\delta)^2$ at the wall distance $d/\delta_{IN} \simeq 0.04$ are compared in the frame (b) and (c), respectively. As can be seen from the frame (a), the DNS data shows that, over the lower convex surface, the TKE

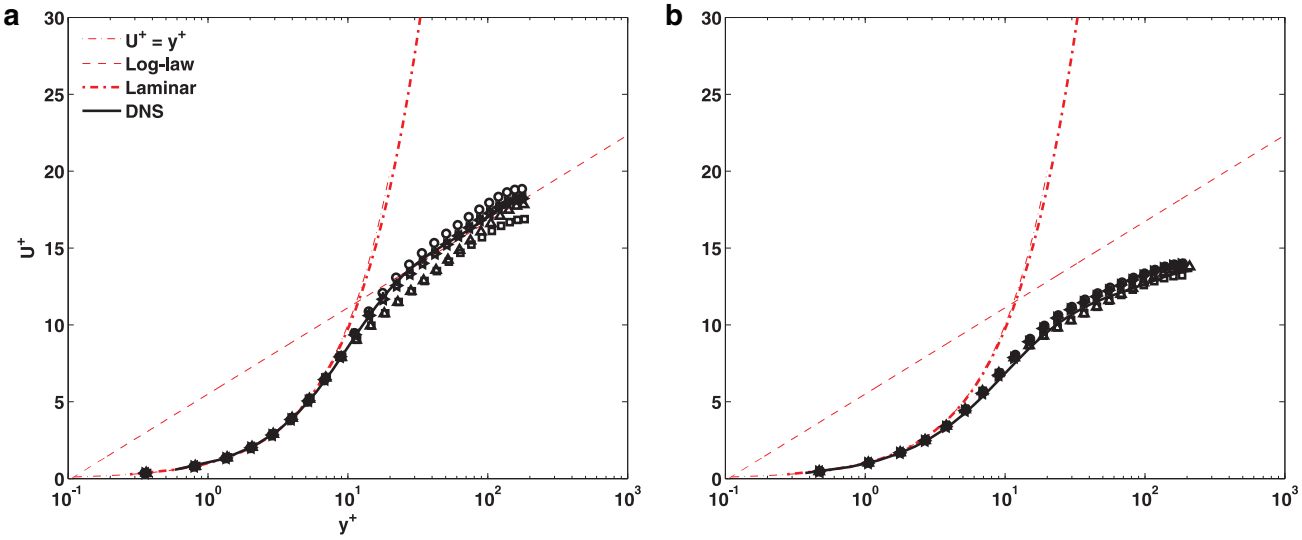

Fig. 5. Mean streamwise velocity profiles in logarithmic abscissa at the streamwise locations, S0 (a) and S1 (b). (– the DNS, –. the laminar, ◦ the RSM, □ the $k-\omega$ SST, △ the $k-\omega$ standard, ▷ the S-A with the strain–vorticity correction, ◁ the S-A standard, and + the HYDRA S-A with the strain–vorticity correction).

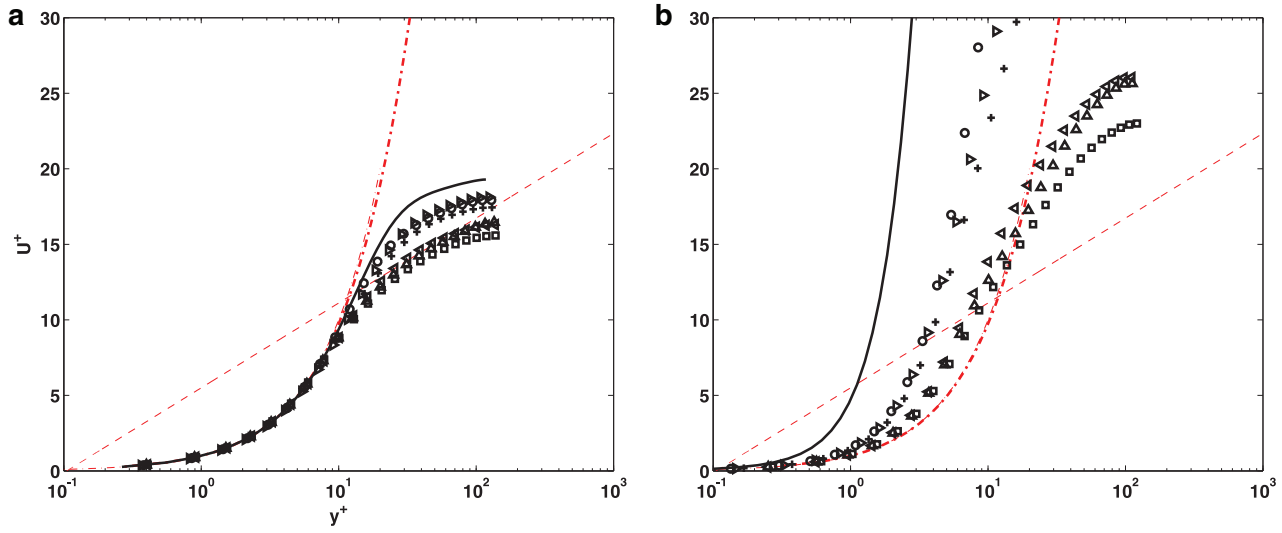

Fig. 6. Mean streamwise velocity profiles in logarithmic abscissa at the streamwise locations, S2 (a) and S3 (b). (– the DNS, –. the laminar, ○ the RSM, □ the $k-\omega$ SST, △ the $k-\omega$ standard, ▷ the S-A with the strain–vorticity correction, ◁ the S-A standard, and + the HYDRA S-A with the strain–vorticity correction).

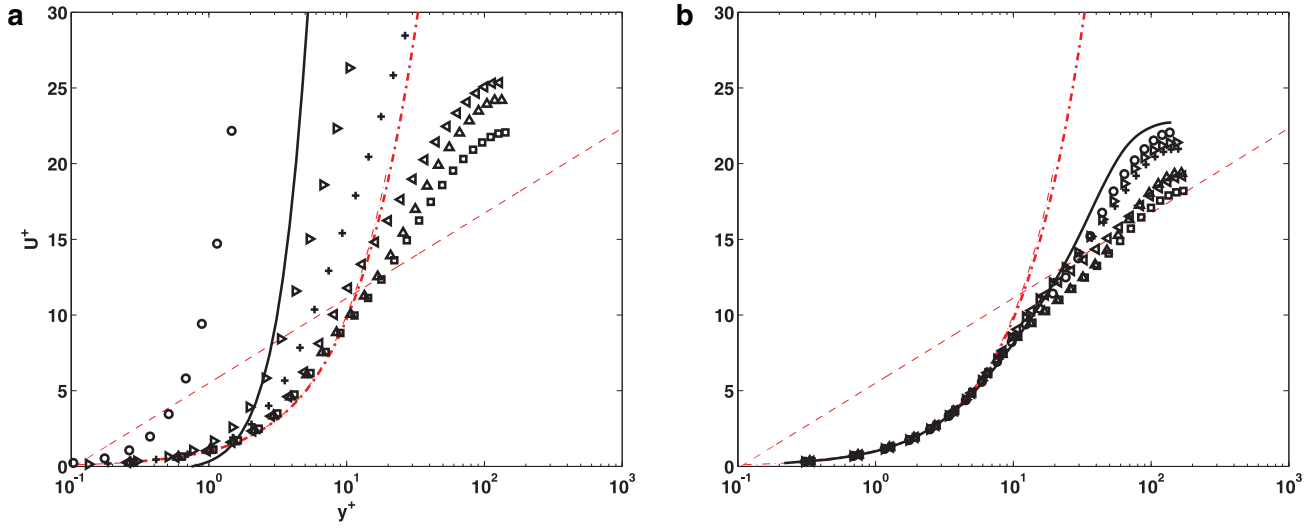

Fig. 7. Mean streamwise velocity profiles in logarithmic abscissa at the streamwise locations, S4 (a) and S5 (b). (– the DNS, –. the laminar, ○ the RSM, □ the $k-\omega$ SST, △ the $k-\omega$ standard, ▷ the S-A with the strain–vorticity correction, ◁ the S-A standard, and + the HYDRA S-A with the strain–vorticity correction.).

is substantially reduced through the laminarisation process. Thereafter, it grows almost linearly through the mean separation, until the induced transition occurs. On the other hand, through the upper concave surface, TKE is substantially enhanced. These characteristic trends are qualitatively captured by the RSM predictions, even though the accuracy needs to be improved. In contrary, the tested eddy-viscosity models do not have the corresponding modelled mechanism to reflect such curvature effects as indicated by the K_S^E and Ri. For RANS results, the corresponding spatial distributions of Ri and K_S^E are shown in Figs. 11 and 12, respectively. The general patterns of these RANS predictions are qualitatively similar to those of the DNS data [33], except for the detailed discrepancies as shown in the frame (b) and (c) of Fig. 10, for example.

Finally, as introduced earlier, the DNS [33] shows that the large streamline curvature can result in highly complex flow physics, particularly the underlying turbulence lagging mechanism and the stress strain misalignment. As described above, the benchmark results show that, overall, the seven-equation RSM model (five-equation in two-dimension) provides better predictions than the eddy-viscosity models. To certain degree, they are able to reflect the laminarisation and the succeeding separation over the lower convex channel wall; whereas, without the corresponding correction, the one/two-equation models are of inadequate sensitivity to such flow physics. On the other hand, all the models are inadequate for accurately capturing the correct trend for the wall shear stress distribution over the concave side with respect to that over the convex. Also, the substantial difficulty arises when predicting the turbulence recovery process through the separation induced transition.

For the current case, the flow has to response to an impulse/step change in streamline curvature. This results in sudden changes in mean strain rate and extra rates of strain, such that the Boussinesq approximation is questionable. Equivalently, for such flow, the assumption that the Reynolds stresses change at a rate proportional to the mean strain rate is not exact. The mean flow processes and time scales are directly related to the channel geometry; whereas, the changes of turbulence properties are lagging to the sudden mean flow

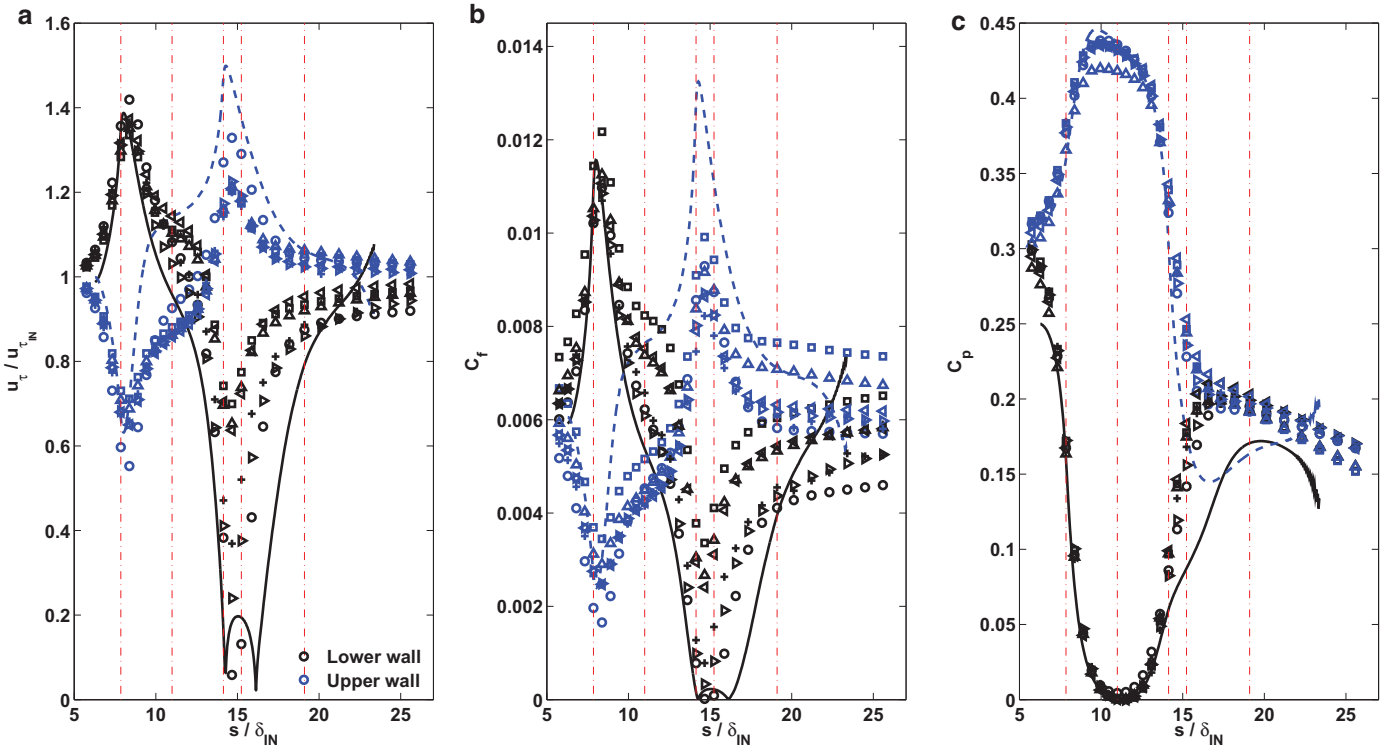

Fig. 8. Streamwise distributions of (a) $u_\tau = \sqrt{\tau_w/\rho}$, (b) $C_f = \tau_w/(0.5\rho U_{max}^2)$, and (c) $C_p = (P - P_{min})/(0.5\rho U_{max}^2)$. (– the DNS, ○ the RSM, □ the $k-\omega$SST, △ the $k-\omega$ standard, ▷ the S-A with the strain–vorticity correction, ◁ the S-A standard, and + the HYDRA S-A with the strain–vorticity correction).

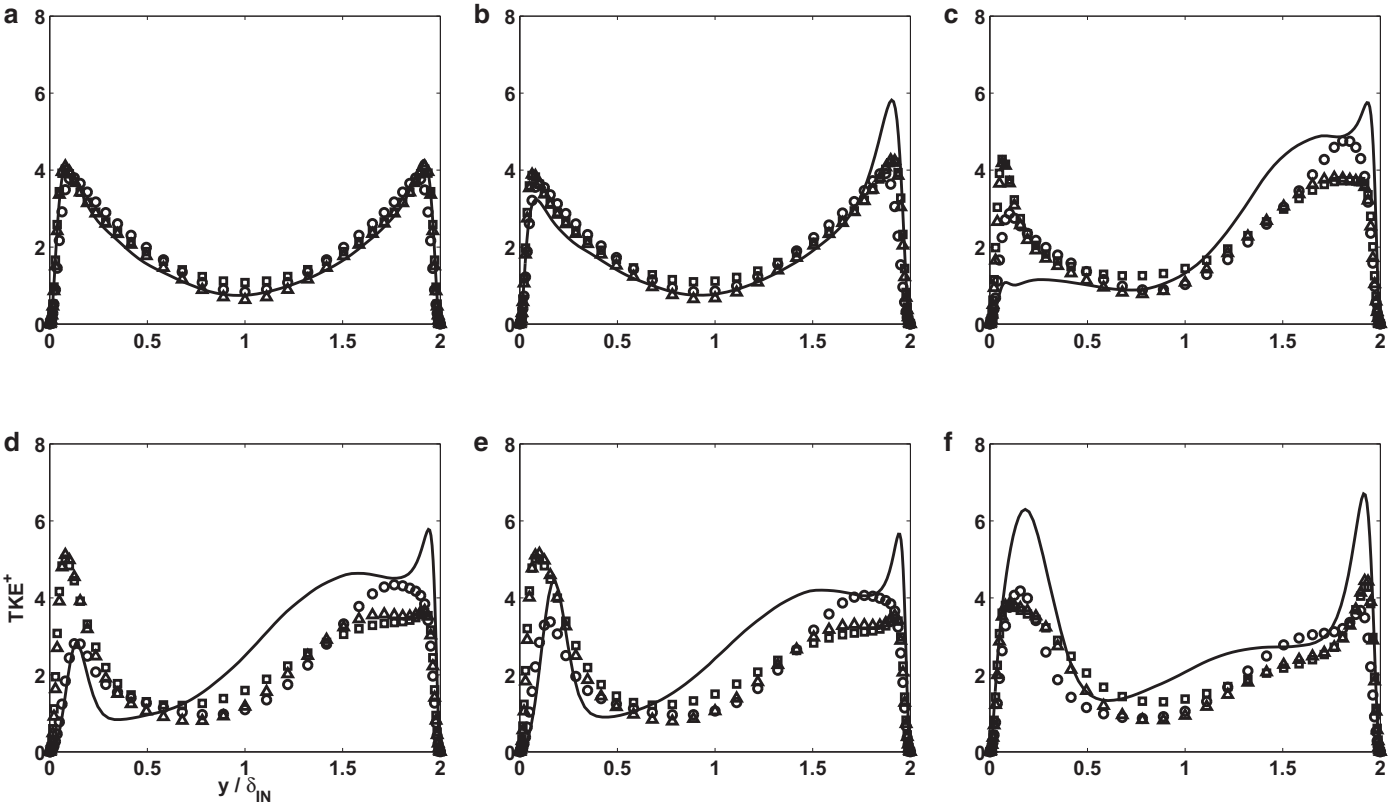

Fig. 9. Turbulence kinetic energy profiles at six streamwise locations. (a) – (f), S0 – S5. (– the DNS, ○ the RSM, □ the $k-\omega$ SST, △ the $k-\omega$ standard).

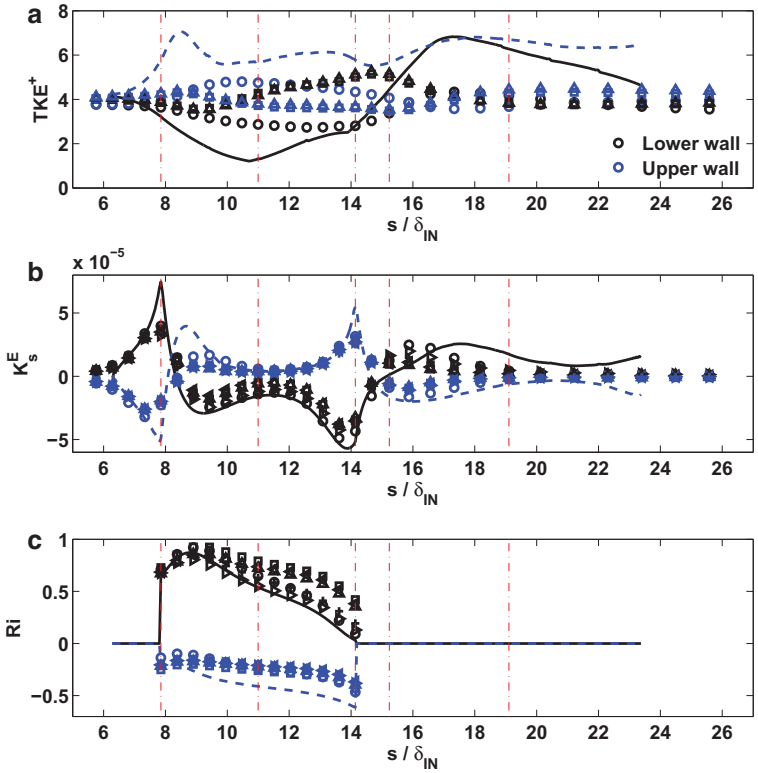

Fig. 10. Streamwise distributions of (a) the peak TKE, and (b) and (c) the mean streamwise acceleration parameter $K_s^E = (\nu_0/U_{max.IN}^2) \cdot (\partial V_s/\partial s)$ and the Richardson number $Ri = (V_s/R) \cdot (\partial V_s/\partial r)/(U_{max.IN}/\delta)^2$ at the wall distance $d/\delta_{IN} \simeq 0.04$. (– the DNS, ○ the RSM, □ the $k-\omega$ SST, △ the $k-\omega$ standard, ▷ the S-A with the strain–vorticity correction, ◁ the S-A standard, and + the HYDRA S-A with the strain–vorticity correction).

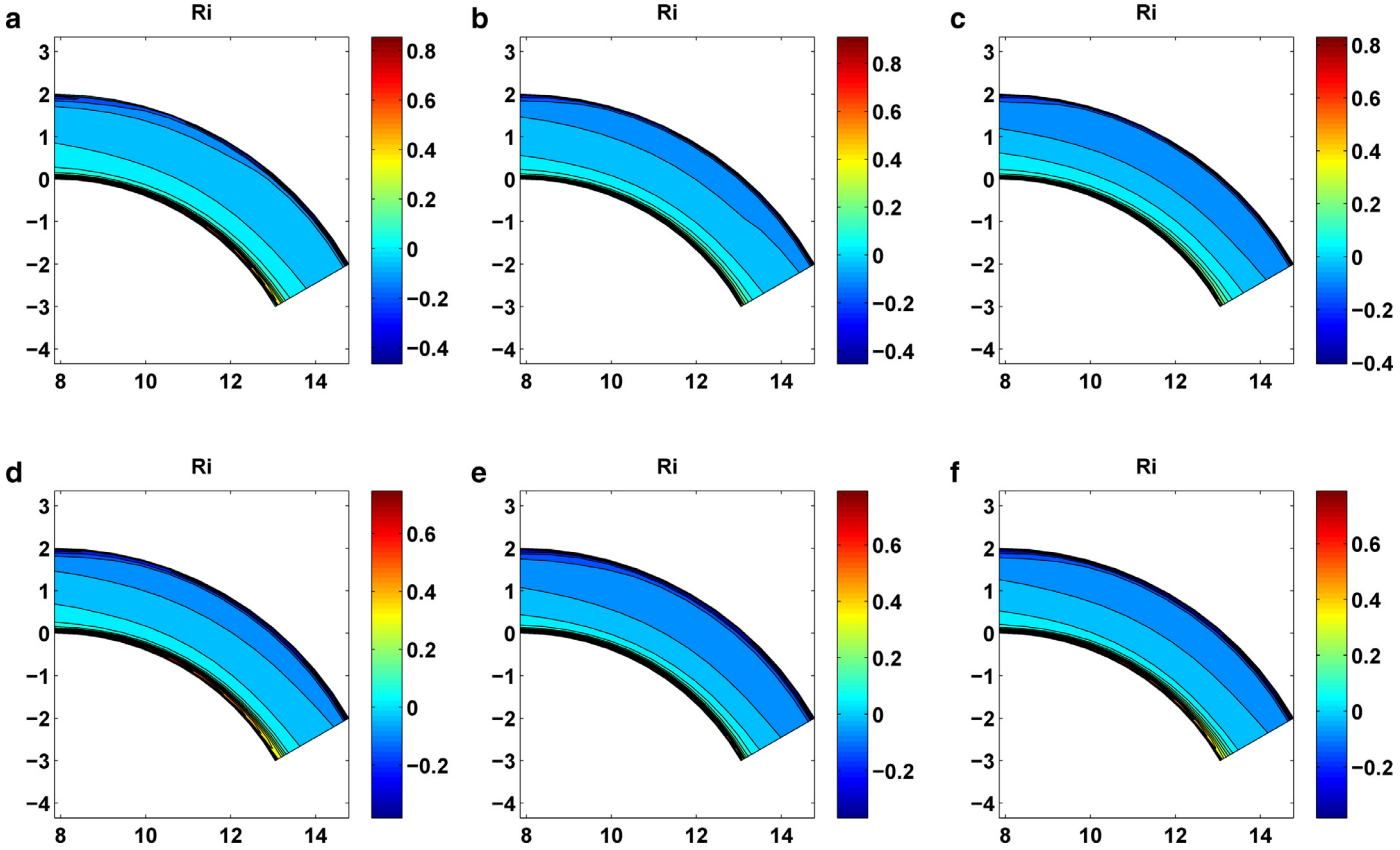

Fig. 11. Spatial distributions of the Richardson number, $Ri = (V_s/R) \cdot (\partial V_s/\partial r)/(U_{max.IN}/\delta)^2$. (The frame (a) – (f) are for the RSM, the SST and the standard $k-\omega$, the S-A with and without the strain–vorticity correction, and the HYDRA S-A models, respectively).

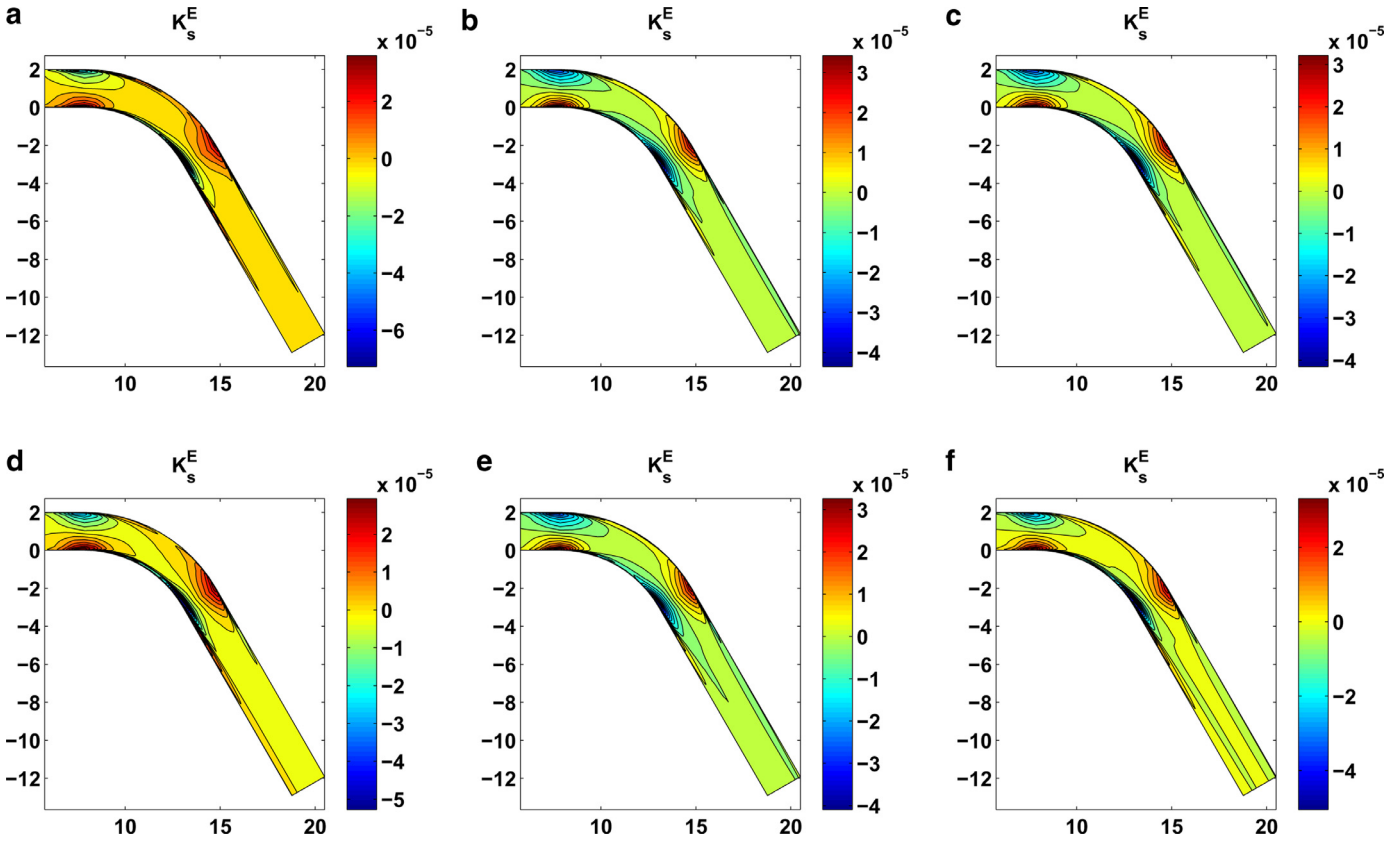

Fig. 12. Spatial distributions of the mean streamwise acceleration parameter $K_s^E = (\nu_0/U_{max,IN}^2) \cdot (\partial V_s/\partial s)$. (The frame (a) – (f) are for the RSM, the SST and the standard $k-\omega$, the S-A with and without the strain–vorticity correction, and the HYDRA S-A models, respectively).

changes. Additionally, as seen from the DNS data [33], the substantial anisotropy of the Reynolds stresses also contradicts such an eddy-viscosity approximation. Therefore, it is not surprising that the predictions of the tested one or two-equation models are unsatisfactory [2–4,21,27,28]. In this case, a non-linear constitutive relation, such as that introduced by Pope [56] and then Gatski and Speziale [57], incorporating with a relaxation approximation, such as that proposed for non-equilibrium flow by Speziale and Xu [58] or Olsen and Coakley [59], may be necessary to represent the anisotropy and the lag mechanism.

On the other hand, for the second-order closure model, even though the flow mechanism is considered to be relatively complete, the closure approximations are mostly calibrated with homogeneous turbulent flows. As shown in the previous section for numerical methods, in addition to the modelled scale-determining equation, for the exact Reynolds-stress transport equations, the dissipation tensor ϵ_{ij}, the turbulent transport tensor C_{ijk}, and the pressure–strain correlation tensor Π_{ij} have to be modelled to close the equations. For the tested low-Re stress-ω model, more elaborate approximations may be used for ϵ_{ij} and C_{ijk}. Nevertheless, the pressure–strain redistribution approximation $\Pi_{ij} = A_{ij} + M_{ijkl} \cdot \partial U_k/\partial x_l$ is perhaps most significant for the current curved channel flow, particularly, the second term for the rapid pressure–strain due to mean strain rate. The corresponding theoretical solution, in terms of appropriate Green's function, is strictly valid only for homogeneous turbulence. Accordingly, this is also the case for the Launder, Reece and Rodi [39] linear approximation for the rapid pressure–strain. Notwithstanding, for inhomogeneous turbulence, particularly as for the current case, the turbulence response to the sudden change of the mean strain rate is clearly not a localised process that can be approximated using a single-point closure. Certain two-point correlations, reflecting the aforementioned lag mechanism, would be more physical [28]. Moreover, for this stress-ω formulation, the model parameter C_2, incorporating with the Launder, Reece and Rodi approximation above, is optimised for the sublayer predictions, primarily for the log-law of the wall. This is also questionable over a curved surface (see Figs. 6 and 7. Perhaps, it is these closure approximations that restrict the RSM model's applicability for the current case, assuming the modelled ω equation is only a supplementary error source. It has been shown by Speziale [60] and then Speziale and Xu [58] that the traditional second-order closures based on the pressure–strain correlation above are only justifiable for homogeneous turbulent flows that are near equilibrium. Accordingly, for non-equilibrium turbulence, in limited consistency with the rapid distortion theory [61,62], a new non-equilibrium explicit ASM was developed based on the relaxation time concept on the Reynolds stress anisotropy tensor. Potentially, this seems to lead to a new generation of second-order closure models [58] and also to a remedy for the current case for which the integral length scales are of the channel half height.

6. Conclusion

The Reynolds-averaged Navier–Stokes simulations have been performed for a turbulent channel flow experiencing a 60 degree circular bend. Some widely-used turbulence models are selected to assess the corresponding model performance for the underlying turbulence lagging mechanism and stress strain misalignment, due to large streamline curvature. These available models include the second-order closure with the stress-ω formulation, the standard $k-\omega$ and the Menter's SST models, the standard Spalart–Allmaras model with and without the corresponding strain–vorticity correction. As expected, comparisons with the DNS data show that, overall, the Reynolds-stress model produces better predictions than the eddy-viscosity models. However, the model accuracy needs to be

further improved. Particularly, the linear approximation for the rapid pressure–strain correlation is considered as the primary source of the model error. This is because such closure approximations are applicable to homogeneous turbulent flows that are nearly equilibrium. But, for the current case, the impulse response of the mean flow to the step change of streamline curvature results in sudden changes in mean strain rate and extra rates of strain. Whereas, the response of the turbulence structures is lagging to these mean flow changes. For the eddy-viscosity models, this also leads to the Boussinesq approximation questionable. Evidently, a non-linear constitutive relation or second-order closure, incorporating with certain relaxation approximation for the lagging mechanism, may be necessary for the current non-equilibrium flow. Also, as seen, the sensitisation to the impact of the large integral length scales would be beneficial for all models.

Acknowledgements

The authors would like to acknowledge the EPSRC and Rolls Royce for their financial support, as well as the U.K. Turbulence Consortium. They would also like to thank all their colleagues at the University of Cambridge, especially Prof. Stewart Cant, Dr. Richard J. Jefferson-Loveday, Dr. Martin N. Goodhand, Dr. Nagabhushana Rao Vadlamani, Dr. Ugochukwu R. Oriji, and Dr. Iftekhar Z. Naqavi for their contributions to the research.

References

[1] Bradshaw P. Effects of streamline curvature on turbulent flow. AGARD-AG-169, AGARDograph 169.
[2] Bradshaw P. Review — complex turbulent flow. J Fluids Eng 1975;97:146–54.
[3] Bradshaw P. In: Koiter WT, editor. Complex turbulent flows in theoretical and applied mechanics. North Holland Pub. Co.: North Holland; 1976. p. 103.
[4] Smits AJ, Young STB, Bradshaw P. The effect of short regions of high surface curvature on turbulent boundary. J Fluid Mech 1979;94:209–42.
[5] Smits AJ, Eaton JA, Bradshaw P. The response of a turbulent boundary layer to lateral divergence. J Fluid Mech 1979;94:243–68.
[6] So RMC, Mellor GL. An experimental investigation of turbulent boundary layers along curved surfaces. NASA CR-1940.
[7] So RMC. A turbulence velocity scale for curved shear flows. J Fluid Mech 1975;70:37–57.
[8] So RMC, Mellor GL. Experiment on turbulent boundary layers on a concave wall. Aero Q 1975;26:25–40.
[9] So RMC, Mellor GL. Experiment on convex curvature effects in turbulent boundary layers. J Fluid Mech 1973;60:43–62.
[10] Richardson LF. The supply of energy from and to atmospheric eddies. Proc R Soc A Lond 1920;97:354–73.
[11] Bradshaw P. The analogy between streamline curvature and buoyancy in turbulent shear flow. J Fluid Mech 1969;36:177–91.
[12] PrandtlL.. Sonderdruck aus Vortrage aus dem Gebiete der aerodynamik und verwandter gebiete. Aachen.Translation NACA Technical Memorandums No 625.
[13] WilckenH.. Effect of curved surfaces on turbulent boundary layers. NASA TT-F-11 421.
[14] Wattendorf FL. A study of the effect of curvature on fully developed turbulent flow. Proc R Soc A Lond 1935;148:565.
[15] Monin A.S., Oboukhov A.M.. Trudy geofiz. inst.AN SSSR1954; 24:163–187.
[16] So RMC, Mellor GL. Turbulent boundary layers with large streamline curvature effects. J Appl Math Phys 1978;29:102–22.
[17] So RMC. Heat transfer modeling for turbulent shear flows on curved surfaces. J Appl Math Phys 1981;32:77–95.
[18] So RMC. On the curvature/buoyancy analogy for turbulent shear flows. J Appl Math Phys 1980;31:96–101.
[19] Wilcox DC, Chambers TL. Streamline curvature effects on turbulent boundary layers. AIAA J 1977;15:574–80.
[20] von Karman T. Some aspects of the turbulence problem . In: Proceedings of International Congress of Applied Mechanics. Cambridge University Press: Cambridge; 1934. p. 54.
[21] Wilcox DC. Turbulence Modeling for CFD. California: DCW Industries; 1994.
[22] Launder BE, Priddin CH, Sharma BI. The calculation of turbulent boundary layers on spinning and curved surfaces. ASME J Fluids Eng 1977;99:231.
[23] Gibson MM, Jones WP, Younis BA. Calculation of turbulent boundary layers on curved surfaces. Phys Fluids 1981;24:386.
[24] Lakshminarayana B. Turbulence modeling for complex shear flows. AIAA J 1986;24:1900–17.
[25] Moser R. D., Moin P. Direct numerical simulation of curved turbulent channel flow. NASA-TM-85974
[26] Moser RD, Moin P. The effects of curvature in wall-bounded turbulent flows. J Fluid Mech 1987;175:479–510.
[27] Wilcox DC. Turbulence modeling for CFD. 2nd ed. California: DCW Industries; 1998.
[28] Wilcox DC. Turbulence modeling for CFD. 3rd ed. California: DCW Industries; 2006.
[29] Patel VC, Sotiropoulos F. Longitudinal curvature effects in turbulent boundary layers. Prog. Aerosp Sci 1997;33:1–70.
[30] Piquet J, Patel VC. Transverse curvature effects in turbulent boundary layer. Prog Aerosp Sci 1999;35:661–72.
[31] Leschziner M. Modelling separation from curved surfaces with anisotropy-resolving turbulence closures ... and related observations on Large Eddy Simulation. In: Janos Vad, Tamas Lajos, Rudolf Schilling, editors. Modelling fluid flow: the state of the art; 2004. p. 23–47.
[32] Oriji UR, Tucker PG. Modular turbulence modelling applied to an engine intake. J Turbomach 2013;136:051004.
[33] Xiaoyu Yang, Numerical investigation of turbulent channel flow subject to surface roughness, acceleration, and streamline curvature, [Ph.D thesis], Department of Engineering, University of Cambridge.
[34] Tucker PG. Trends in turbomachinery turbulence treatments. Prog Aerosp Sci 2013;63:1–32.
[35] Yang X, Tucker PG. Assessment of turbulence model performance: severe acceleration with large integral length scales. Comput Fluids 2015.in press
[36] Spalart PR, Shur M. On the sensitization of turbulence models to rotation and curvature. Aerosp Sci Technol 1997;5:297–302.
[37] Shur ML, Strelets MK, Travin AK, Spalart PR. Turbulence modeling in rotating and curved channels: assessing the spalart-shur correction. AIAA J 2000;38:784–92.
[38] Launder BE, Shima N. Second-moment closure for the near-wall sublayer: development and Application. AIAA J 1989;27:1319–25.
[39] Launder BE, Reece GJ, Rodi W. Progress in the development of a Reynolds-stress trubulence closure. J Fluid Mech 1975;68:537–66.
[40] Launder BE. Second-moment closure and its use in modeling turbulent industrial flows. Int J Numer Methods Fluids 1989;9:963–85.
[41] Launder BE. Second-moment closure: present ... and future. Int J Heat Fluid Flow 1989b;10:282–300.
[42] Menter FR. Two-equation eddy-viscosity turbulence models for engineering applications. AIAA J 1994;32:1598–605.
[43] Menter FR., Rumsey CL. Assessment of two-equation turbulence models for transonic flows. AIAA-94-2343.
[44] Menter FR, Kuntz M, Langtry R. Ten years of experience with the SST turbulence model. In: Hanjalic K, Nagano Y, Tummers M, editors. Turbulence, heat, and mass transfer; 2003. p. 625–32.
[45] Menter FR. Review of the SST turbulence model experience from an industrial perspective. Int J Comput Fluid Dyn 2009;23:305–16.
[46] Spalart PR, Allmaras SR. A one-equation turbulence model for aerodynamics flows. La Rech Aerosp 1994;1:5–21.
[47] Dacles-Mariani J, Zilliac G, Chow J, Bradshaw P. Numerical and experimental study of a wingtip vortex in the near field. AIAA J 1995;33:1561–8.
[48] ANSYS. Fluent theory guide. Canonsburg, PA 15317, USA: ANSYS Inc., Southpointe; 2011.
[49] Nichols RH. Turbulence models and their application to complex flows (version 4.01). University of Alabama at Birmingham; 2014.
[50] Kolmogorov AN. Local structure of turbulence in incompressible viscous fluid for very large Reynolds number. Dokl Akad Nauk SSSR 1941;30:299–303.
[51] Daly BJ, Harlow FH. Transport equations in turbulence. Phys Fluids 1970;13:2634–49.
[52] Rotta JC. Statistische theorie nichthomogener turbulenz. Z Phys 1951;129:547–72.
[53] Rotta JC. Turbulent boundary layers in incompressible flow. In: Ferri A, Kuchemann D, Sterne LHG, editors. Progress in aeronautical sciences, vol. 2; 1962. p. 1–221.
[54] Lapworth L, Shahpar S. Design of gas turbine engines using CFD. In: Proceedings of European Congress on Computational Methods in Applied Sciences and Engineering, ECCOMAS; 2004.
[55] Lapworth L. The challenges for Aero-Engine CFD. ICFD 25th Anniversary Meeting. Derby, UK.
[56] Pope SB. A more general effective viscosity hypothesis. J Fluid Mech 1975;72:331–40.
[57] Gatski TB, Speziale CG. On explicit algebraic stress models for complex turbulent flows. J Fluid Mech 1993;254:59–78.
[58] Speziale CG, Xu XH. Towards the development of second-order closure models for nonequilibrium turbulent flows. Int J Heat Fluid Flow 1996;17:238–44.
[59] OlsenM.E., CoakleyT.J.. The lag model, a turbulence model for non-equilibrium flow. 2001AIAA paper 2001-2564.
[60] Speziale CG. A review of Reynolds stress models for turbulent shear flows. ICASE Report No. 95-15, NASA-CR-195054; 1995.
[61] Tucker PG, Liu Y. Turbulence modeling for flows around convex features giving rapid eddy distortion. Int J Heat Fluid Flow 2007;28:1073–91.
[62] Hunt JCR. A theory of turbulent flow round two-dimensional bluff bodies. J Fluid Mech 1973;61:625–706.